PGM-free metal oxide nanoarray forests for water-promoted low-temperature soot oxidation

Chunxiang Zhu [a,1], Shoucheng Du [a,1], Sibo Wang [a], Xingxu Lu [a], Mingwan Zhang [a], Bo Zhang [a], Fangyuan Liu [a], Wen Xiao [b], Yanbing Guo [c], Jun Ding [b], Zhaoliang Zhang [d], Pu-Xian Gao [a,*]

[a] Department of Materials Science and Engineering & Institute of Materials Science, University of Connecticut, Storrs, CT 06269-3136, USA
[b] Department of Materials Science & Engineering, National University of Singapore, Singapore 117574, Singapore
[c] Institute of Environmental Chemistry, College of Chemistry, Central China Normal University, Wuhan 430079, China
[d] School of Chemistry and Chemical Engineering, University of Jinan, Jinan 250022, China

ARTICLE INFO

ABSTRACT

In this study, PGM free metal oxide based nanorod array (nanoarray) forests have been conformally integrated onto the millimeter-sized channel walls and microscale pores of SiC diesel particulate filter (DPF) substrates using scalable microwave-assisted hydrothermal and dip-coating methods. High-efficiency and robust low temperature soot oxidation is successfully achieved using such a new type of cDPFs as a result of i) promoted tight soot-catalyst contact through spontaneous soot deposits in-between nanorods, ii) highly dispersed loading of $LaSrCoO_3$ perovskite oxidation catalysts onto ZnO nanorod arrays, effectively mitigating active site blockage by soot deposition. The light-off temperature of soot oxidation was lowered to 250 °C in oxygen, a 250 °C decrease compared to that of the commercial Pt based catalyst, due to the abundant oxygen vacancies enabled by the $LaSrCoO_3$/ZnO (LSCO/ZnO) nanorod array catalysts. The performance of the catalyst was further enhanced to initiate the soot oxidation at ~150 °C with co-fed gas of NO, due to the LSCO catalyzed NO_2 formation and its favorable oxidation with soot at low temperature. Furthermore, the nanoarray supported perovskite catalyst shows excellent stability and activity after 120 h of hydrothermal aging at 650 °C. Soot oxidation T_{max} is lowered from 542 °C to 510 °C under 6 % water steam condition due to the formation and promotion effect of oxidative -OH species. *In situ* DRIFTS study reveals that such -OH species form at various catalyst surfaces and interfaces, pointing to a potentially generic water promotion effect for solid/solid interfacial catalytic oxidation under humidity condition. Finally, the mechanistic soot oxidation pathways under O_2, NO_2, and H_2O feeds are proposed for understanding the low-temperature soot oxidation behaviors over the nanoarray supported perovskite catalysts.

1. Introduction

Soot is a complex carbon-containing solid by-product generated during combustion of diesel or gasoline. Large particles (>10 μm), such as dust, can be filtered through human body protective systems such as the upper respiratory tract, while soot can penetrate the respiratory tract with a size ranging from tens of microns to tens of nanometer, causing major health concerns [1,2]. New measurement has been applied to diesel vehicles according to the Euro 6 legislation for stringent limitation of soot emissions [3]. Besides, the Euro 6c legislation also required strictly limited soot emissions for gasoline engines, expediting the research need on efficient gasoline particulate filters (GPFs) [4].

Channel structured honeycomb based particulate filters were developed for filtration of soot from diesel engine emissions through wall flow structures, and are considered promising as GPFs as well. During filtration, the accumulation of soot on the porous filter walls and inner pore surfaces induces increased pressure drop, resulting in decreased power efficiency and fuel economy, and environmental pollution if the filters are not cleaned regularly [5,6]. Thus, regular regeneration through oxidizing soot is a must to maintain the filtration efficiency of the GPFs or DPFs and the overall vehicle performance.

Regeneration of the accumulated soot can be performed either in

active mode, where extra fuel and heat are actively applied, or in passive mode, where soot oxidation takes place over catalysts without any active interference to raise the exhaust temperature [5]. Active DPF regeneration is currently widely adopted in diesel engine vehicles, where the exhaust temperature is relatively low compared to the gasoline engine ones. An extra fuel injection process is usually performed during an active regeneration, steeply increasing the exhaust temperature by exothermic combustion of the excessive fuel. It is argued that this strategy could lead to more exhaust due to significant extra emissions generated, and compromised fuel economy [6]. Therefore, the design and implementation of low temperature soot oxidation catalysts have been under intensive investigation for efficient passive DPF regeneration.

The efficiency of passive DPF regeneration is closely associated with the activity and utilization of the active sites, as influenced by catalyst-soot contact, catalyst morphology, surface area, etc. [7]. Different catalysts, such as noble metals [8,9], alkali and alkaline earth metal oxides [10,11], perovskites [12–14], ceria-based [15–17] and manganate-based [18] materials have been investigated. For example, perovskite catalysts have been proposed as substitutes for noble metal-based catalysts, showing low-cost, high thermal and hydrothermal stability, and remarkable activity in soot oxidation [19–21]. However, one limitation associated with the above-mentioned catalysts is that they were synthesized in powder-form and then wash-coated to the wall-flow substrates, which results in a "loose contact" scenario between soot and catalyst surface [22] (Fig. 1a). The accumulated soot particles that are not in contact with catalyst surface can only be non-catalytically combusted at high temperature. To improve this, recently, Fang et al. [23] has developed perovskite nanofiber web-based catalysts to increase the catalyst surface roughness, enhancing the contact between catalyst and soot (Fig. 1b). Another approach for enhancing soot and catalyst contact is to use fuel additives, where catalysts are introduced to the fuel. After fuel combustion, the additives (catalysts) are encapsulated by soot on the surface, forming a catalyst-core/soot-shell structure, and therefore the soot-catalyst interaction is enhanced [24]. However, this approach introduces the additives as secondary deposits on the DPF and requires a dedicated fueling strategy [25].

Herein, a new type of nanorod array supported perovskite catalytic DPFs has been successfully demonstrated with a remarkable activity for low-temperature soot oxidation. Built on our prior work on nano-array based catalytic converter [26–33], instead of using wash-coats, we have successfully grown catalytically active materials as nanorod arrays onto the SiC wall-flow structured DPFs (Fig. 1 c). Such a nano-array forest was proved to favor the achievement of catalyst-soot tight contact, allow efficient usage of cost-effective materials [34,35], such as perovskites, as well as enhance uniform dispersion of the active species and mass transfer due to the well-defined nano-array structures [36–38]. With strontium doping, the nanorod array supported perovskite catalyst significantly lowered soot oxidation light-off temperature by 250 °C, i. e., from 500 °C to 250 °C, as compared to the commercial bench-mark catalyst. The light-off temperature was further decreased to about 150 °C under the simulated exhaust where NO presents. Moreover, the catalyst also demonstrates promoted soot oxidation capability and good stability under 6 % of H_2O condition after 120 h of hydrothermal aging at 650 °C.

2. Experimental methods

2.1. Microwave assisted nanorod array synthesis

In ZnO seeding, 20 mM [Zn^{2+}] ethanol solution was prepared by dissolving 2.19 g zinc acetate dihydrate ($Zn(Ac)_2 \cdot H_2O$) in 500 ml ethanol. A clean SiC substrate with the dimension of 6.35 cm (diameter) × 2.54 cm (channel length) was submerged in the seeding solution and sonicated for 1 min. Then the substrate was immediately dried under microwave irradiation. The cycle was repeated about 10 times until desired quantity of precursors was deposited on the substrate surface. Calcination was performed in a furnace at 350 °C for 2 h for crystallized ZnO seeds. The substrate was then vertically mounted in a glass reactor located in a laboratory microwave oven (BP-125). A peristaltic pump was used to pump the 12.5 mM solution prepared by dissolving equal molar zinc acetate dihydrate ($Zn(Ac)_2 \cdot H_2O$) and hexamethylenetetramine (HMT) in DI water through the substrate channels at a flow rate of 100 ml/min. The solution was maintained at 90 °C, monitored by a thermocouple. After 2 h, the substrate was taken out, cleaned in ethanol under sonication for 5 min, and dried in air at 90 °C.

2.2. Perovskite coating

The perovskite sol-gel solution with targeted composition of La$_{1-x}$Sr$_x$CoO$_3$ (x = 0.2, 0.4, 0.6) was prepared by dissolving stoichiometric La(NO$_3$)$_3 \cdot 6 H_2O$, Sr(NO$_3$)$_2$, and Co(NO$_3$)$_2 \cdot 6H_2O$ in 20 ml N, N-Dimethylformamide (DMF) under sonication. The Co(NO$_3$)$_2 \cdot 6H_2O$ concentration was kept at 0.12 M for all solutions. 2 g polyvinylpyrrolidone (M.
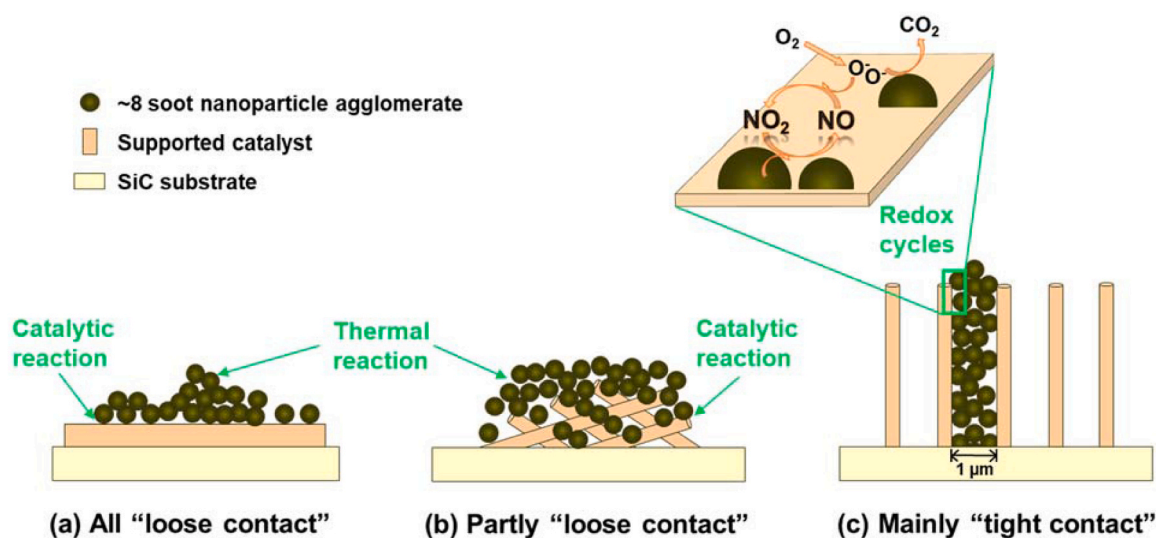

Fig. 1. Comparison of (a) a typical supported catalyst washcoated on SiC substrate, (b) a modified rough surface supported catalyst washcoated on SiC substrate, and (c) a nanorod array supported catalyst grown on SiC substrate, as well as the associated soot oxidation redox cycles.

W. 55,000) and 0.5 ml diethanolamine were dissolved in another 20 ml DMF in sonication. The two prepared solutions were fully mixed under vigorous stirring at 60 °C and the solution gradually turned dark purple. The achieved solution was then aged at the room temperature for 24 h. The as-prepared ZnO nanorod array integrated SiC substrate with the dimension of 2 cm × 1 cm × 1 cm was soaked into the colloidal solution under sonication. The excessive solution in substrate channels was removed by the compressed air. The sample was then transferred to a microwave oven, and dried under the microwave irradiation. After the sample was completely dry, it was calcined at 350 °C for 5 min before the next coating cycle. This deposition procedure was repeated several times until 15 wt % loading was reached. The final calcination step was carried out at 700 °C for 2 h at a heating rate of 5 °C/min.

A schematic flow diagram that describes the whole synthesis process is shown in Scheme S1.

2.3. Hydrothermal aging

To test the long-term stability of the catalyst, an accelerated hydrothermal aging process was performed under 5 % O_2, 5 % CO_2, 6 % H_2O, balanced with N_2 at 650 °C for 120 h.

2.4. In situ diffuse reflectance infrared spectroscopy (DRIFTS)

The in-situ DRIFTS study was performed with a Fourier Transform Infrared Spectrophotometer (Nicolet iS-50 FTIR Spectrometer, Thermo Scientific). For sample preparation, the monolithic catalysts were crushed into powder form and mixed with KBr with 10 wt % of catalyst. Signal was collected in the wavenumber range of 600–4000 cm^{-1} with 64 scans at a resolution of 4 cm^{-1}. To offset the signal drift caused by temperature, background spectrums were collected at each temperature (50, 200, 300, 400 and 500 °C) with N_2 purging, then applied to each temperature test. NO was added by a separate stream controlled with a mass flow controller. Water was introduced by bubbling a stream of N_2 through a saturator. The content of water can be varied by controlling the saturator temperature.

2.5. Materials characterization

The X-ray diffraction patterns on the prepared nanorod array structures were acquired using a BRUKER D2 X-ray diffractometer (Cu Kα radiation, λ = 1.540598 Å) with an operating beam voltage of 30.0 kV, and a beam current of 10 mA. The morphology and structure of nanorod array catalysts were characterized using a field-emission SEM (FEI Nova NanoSEM 450) at an accelerating voltage of 15.0 kV, and a high-resolution transmission electron microscope (FEI Talos F200X S/TEM, 200 kV). The BET surface areas and pore size distribution of catalysts were determined by nitrogen adsorption/desorption in a Micromeritics ASAP 2020 Accelerated Surface Area and Porosimetry System. The impedance analyses were performed in CHI 6011E electrochemical analyzer (CH Instrument Inc.). Two triangle-shaped electrodes were plugged onto the substrate channel walls with the distance of either three or eight channels in-between. The frequency was scanned from 1 to 10^6 Hz. X-ray photoelectron spectroscopy (XPS) spectra were measured in Kratos Analytical (Axis Ultra DLD). The X-ray radiation was generated by a monochromatic Al Kα source operating at photon energy of 1486.7 eV. The signal of photoelectron was filtered by a hemispherical analyzer with pass energy of 160 eV and 20 eV for survey scan and narrow high-resolution scans, respectively. C1s photoelectron line at 284.6 eV was adopted as internal standard for spectra calibration to compensate charging effect. H_2-temperature programmed reduction (H_2-TPR) was carried out in a ChemiSorb 2720 Pulse Chemisorption System. Each structured perovskite/ZnO catalyst was placed in the reactor without treatment. Specifically, 2 × 2 channels were cut by a blade and loaded in the U shape quartz tube for H_2 programmed reduction. The catalyst was heated from the room temperature to 800 °C

at a heating rate of 10 °C/min under 25 sccm gas flow of 4 % H_2 balanced in N_2.

2.6. Reactor setup and performance evaluation conditions

Carbon black was used as soot model compound and loaded onto the modified DPFs by a dip coating method. Commercial carbon black generated from acetylene decomposition was purchased from Alfa Aesar. The carbon black has the following properties: 50 % compressed, 99.9+ % purity, bulk density: 112 g/L, moisture content: 0.055 %, ash content: 0.005 %, surface area: 75 m^2/g. The morphology, the elemental fractions as well as the approximate particle size (~40 nm) of the carbon black are shown in Fig. S1 of the Supporting Information. In the loading process, carbon black was suspended in Ethylene Glycol (EG) with the concentration of 6 mg carbon/ml EG. The prepared structured catalysts or the commercial one was submerged into the carbon suspended solution under sonication, and then taken out and dried at 250 °C for 2 h. Soot oxidation under different gas atmospheres (O_2 or NO/O_2) was performed in a horizontal quartz tube reactor. Before experiments, catalysts of the same volume (0.8 cm × 0.8 cm × 1 cm length) were loaded into the reactor. The catalysts were wrapped with insulation wools for fixed position in the quartz tube and convective flow through the catalyst channels. A K-type thermocouple was inserted into the reactor for in-situ measurement of the catalyst bed temperature. 8 % O_2 balanced in N_2 was used for soot oxidation in O_2, whereas 200 ppm NO and 8 % O_2 balanced in N_2 was used for soot oxidation in O_2/NO. A total gas flow rate of 500 sccm (~47,000 hr^{-1} space velocity) was maintained for all the experiments, as recommended by an industrial testing protocol [39]. For tests subjected to moisture, water was introduced by bubbling a stream of N_2 through a temperature-controlled saturator. Fourier transform infrared spectrometer (FTIR, Thermo-fisher Nicolet 6700) was calibrated using gas standards and used for on-line analysis of gas components. All the experiments were repeated at least twice to justify the accuracy of the experiments.

3. Results and discussions

3.1. Development and characterization of nanorod array based DPFs

So far, a great deal of effort has been made on development of the nanorod array based structured catalysts [40–42]. Using the hydrothermal deposition route as illustrated in Scheme S1, ZnO nanorod arrays were grown on the commercial SiC wall flow honeycomb substrate (Fig. 2a-e). The grown nanorod arrays have a well-defined geometry with uniform size and orientation (Fig. 2b and d). Such geometries provide possibilities to reveal exact material structure–property correlations, which further assists rational catalyst design and optimization. The three-dimensional array structure could effectively decrease the chances of active site agglomerating, thus enhancing the dispersion of active species and leading to more active and accessible active sites for soot oxidation. All the characterizations and tests are based on the freshly made catalyst without hydrothermal aging unless further stated.

Fig. 2c and e show the SEM images of the nanorod arrays with perovskite coated as the "shell". The perovskite loading was controlled uniformly for all the catalysts used in this study, as summarized in Table 1. The surface La/Sr ratio of the perovskites was examined by Energy Dispersive X-ray spectroscopy (EDX), with the trend consistent to the Sr doping expected during the synthesis. In Table 1, the $Sr_{surface}$ could be attributed to the formation $SrCO_3$, SrO, and $Sr(OH)_2$ [43,44]. As Sr doping ratio increases, the lattice Sr fraction gradually increases, suggesting that the doping method used in this study could effectively populate the lattice Sr. Table 1 also summarizes grain size, BET surface area and BJH adsorption average pore diameter of the synthesized LSCO/ZnO catalysts (See Fig. S2 for N_2 ad-/de-sorption isotherms and pore size distribution). The grain size and the pore size of the nanorod array were increased, and the BET surface area was decreased by the
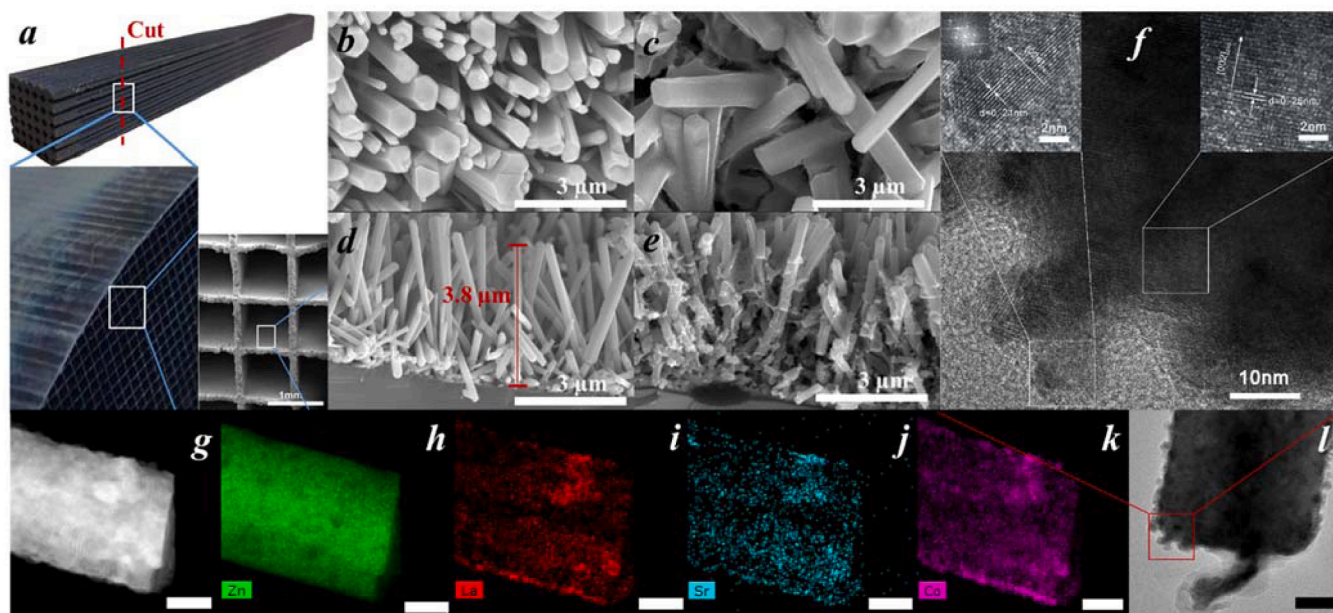
Fig. 2. (a) Images of commercial SiC wall-flow substrate and (b-e) SEM images of ZnO nanorod arrays on SiC substrate (b, d) before and (c, e) after $La_{0.8}Sr_{0.2}CoO_3$ (LSCO) perovskite coating. (f) HRTEM, (l) bright field, (g) HAADF, (h-k) elemental mapping characterizations of a LSCO/ZnO composite nanorod array. Scale bars represent 50 nm, unless noted otherwise.

Table 1
Physicochemical properties and catalytic performance of the synthesized LSCO/ZnO nanorod array-based catalysts.

	LR[a] (%)	La/ Sr[b]	d_G[c] (nm)	S_{BET}[d] (m^2 g^{-1})	d_{pore}[e] (nm)	SL[f] (wt %)	S/P[g] (wt %)	T_{peak} (°C)	$O_{lattice}$/ O_{ads}[h]	Co^{2+}/ Co^{3+},[h]	$Sr_{surface}$/ $Sr_{lattice}$[h]
$La_{0.4}Sr_{0.6}CoO_3$/ZnO	5.1	1.3	16.6	0.9	45.9	0.42	8.3	403	0.32	0.21	0.50
$La_{0.6}Sr_{0.4}CoO_3$/ZnO	4.4	3.3	13.3	2.1	24.8	0.44	9.9	421	0.44	0.19	0.62
$La_{0.8}Sr_{0.2}CoO_3$/ZnO	4.6	6.5	10.2	5.3	12.8	0.44	9.5	484	0.64	0.18	1.66
ZnO	0	-	-	1.6	10.9	-	-	-	-	-	-
$La_{0.4}Sr_{0.6}CoO_3$/ZnO-Aged	5.2	7.2	16.8	0.75	4.0	0.47	9.0	542	1.16	0.75	0.58

[a] Perovskite loading ratio (LR) was calculated by the mass of perovskite divided by the mass of ZnO nanorod array grown on SiC substrate.

[b] La/Sr atomic ratio of the perovskite sample was analyzed by EDX. The La/Sr ratio tend is consistent to the synthesis solution.

[c] Grain size (d_G) was calculated based on the XRD patterns shown in Fig. S4 of Supporting Information.

[d] BET surface area of the whole DPF, including substrate, ZnO nanorod arrays, and perovskites

[e] BJH adsorption average pore diameter (4 V/A)

[f] Soot loading ratio (SL) was calculated from the mass of soot divided by the mass of DPF. Carbon black was used to model soot (Fig. S1).

[g] Soot to perovskite weight ratio

[h] Ratios were calculated from deconvoluted XPS spectra areas, shown in Fig. 8 and Fig. S12.

increased Sr doping ratio.

Fig. 2f is a high-resolution TEM (HRTEM) image of the tip region of a LSCO/ZnO nanorod array (Fig. 2l). The upper-right inset corresponds to the {002} planes of ZnO with the lattice spacing of 0.26 nm [45]. The upper-left inset corresponds to the {024} planes of LSCO with the lattice spacing of 0.21 nm. The ZnO and LSCO crystalline phases and planes can also be identified from the corresponding XRD spectra summarized in Fig. S4. Good dispersion of the Sr doped perovskite on the ZnO nanorod array is confirmed by the elemental mapping results shown in Fig. 2h-k and Fig. S3 (d-g). The synthesized LSCO/ZnO nanorod array demonstrates good crystallinity, as shown in the inset of Fig. S3 (a, b) and XRD results in Fig. S4.

3.2. Nanorod array enhanced soot oxidation activity

To directly characterize the morphology and distribution of soot particles and nanorod array catalysts, SEM characterizations were conducted. SEM of a commercial DPF (Fig. 3a and c)) exhibits limited roughness and accessibility on the surface compared to the nanorod array structured catalyst (Fig. 3b and d). This implies that soot cannot

contact the catalyst surface in a "tight" mode. Moreover, what can also be expected is that as soot accumulates on the commercial DPF in the practical exhaust situation, a "soot cake" is formed, where most of the soot content is too far away from the catalyst surface to receive the spilled-over oxygens from the catalyst active sites. In contrast, the nanorod array-based catalysts can settle and hold soot nanoparticles in between the inter-nanorod spaces, until the spacing is fully filled up. Such soot-catalyst contact configurations can be characterized by using electrochemical impedance spectroscopy with AC input. As shown in Fig. 4a, when soot loading exceeds 3.2 wt % of ZnO/honeycomb substrate, the "soot cake" starts to form in the wash-coated ZnO/ honeycomb substrate, as reflected by the dramatic decrease of the sample impedance as soot conducts electrons better than ZnO and cordierite honeycomb substrate [46]. It is also clear in Fig. 4a, although not quantified, that the nanorod array-based catalyst has tighter contact with soot due to its three-dimensional structure, which results in lower impedance in the range of 0–1.2 wt %, as compared to the wash-coated counterparts.

Both the "loose" contact and lack of contact area between soot and catalyst surface with the commercial DPF are reflected in the
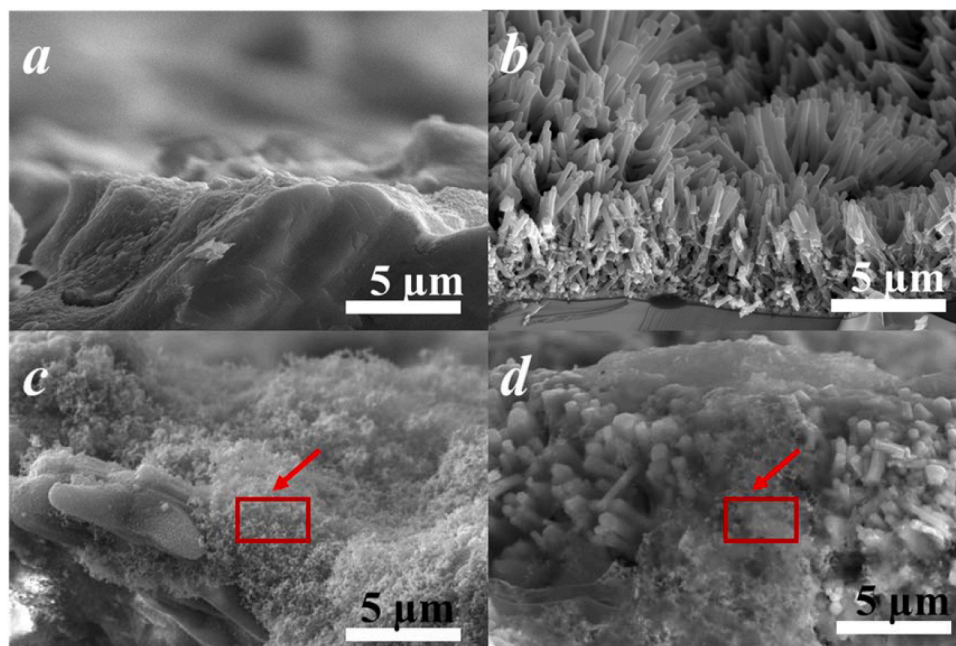
Fig. 3. SEM images of (a, c) commercial washcoated DPF section and (b, d) LSCO/ZnO composite nanorod array based DPF section (a, b) before and (c, d) after carbon black loading. The red arrows point to the fluffy carbon black.
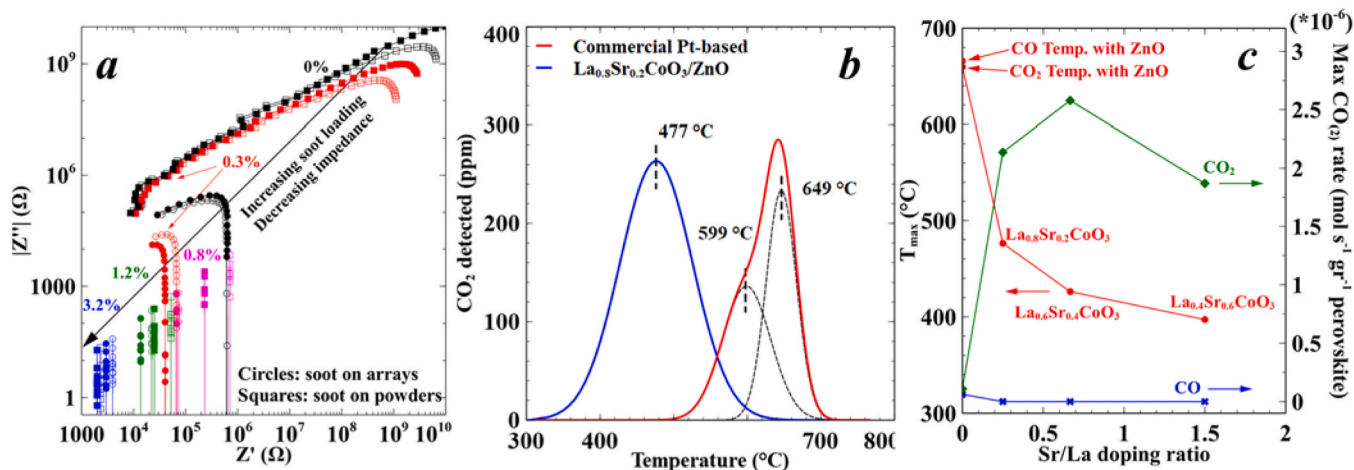

Fig. 4. (a) Nyquist plot for different soot loadings on washcoated ZnO/honeycomb substrate and ZnO nanorod arrays/honeycomb substrate. The filled markers represent measurement across 8 cordierite honeycomb substrate channels; the empty ones 3 channels for verification. (b) Soot oxidation over commercial Pt-based DPF catalyst (0.9 g/L Pt loading) and nanorod array based DPF catalyst. Soot loading amount and method were kept consistent for the comparison. (c) Soot oxidation over LSCO/ZnO nanorod array-based catalysts with different strontium doping ratios and ZnO nanorod array control sample. T_{max} represents the temperature at the peak of the outlet CO_2 concentration profile. CO_2 formation rate was normalized by the mass loading of the perovskite on the nanorod arrays.

performance tests, where two peaks are shown in the outlet CO_2 concentration profile (Fig. 4b). The lower temperature peak is reasonably attributed to the Pt enhanced catalytic oxidation of soot, whereas the higher temperature peak is from thermal (non-catalytic) oxidation of soot, confirmed by the non-catalytic experiment with the parent ZnO nanorod array (Fig. S5). The significantly large peak area of the higher temperature peak is consistent to the "soot cake" claims drawn from the SEM and Impedance analyses (Fig. 3c and Fig. 4a). In contrast, the LSCO/ZnO nanorod array-based catalyst with enriched loading of well-dispersed perovskites as active species demonstrates enhanced soot oxidation activity at a much lower temperature. This is attributed to not only the abundant available oxygen vacancies of the perovskite material for soot oxidation due to larger soot-catalyst contact area, but also rapid transfer of the surface oxygen to soot by the closer contact between soot and the nanorod array catalyst [47,48].

To better demonstrate the advantages of the well-defined 3D nano-array structure, a composite catalyst with similar composition (LSCO-$La_{0.8}Sr_{0.2}CoO_3$, ZnO and SiC) but without nanorod array configuration is prepared using a dip-coating method and tested for soot oxidation. In the dip-coating process, powder form ZnO nanorod supported LSCO is firstly prepared following by a slurry dip-coating of the powder on SiC monolith, and then the same sample aftertreatment conditions are applied as the nanoarray configured samples. Meanwhile, a SiC monolith supported LSCO catalyst is also prepared to demonstrate the high catalytic activity of LSCO perovskite. The soot oxidation performance is summarized and compared over different configurations, namely catalyst with and without nanoarray morphology, and catalyst based on LSCO perovskite or Pt, as shown in Fig. S6a and b. Compared with commercial Pt based catalyst, use of LSCO perovskite catalyst can lower the soot oxidation temperature from 650 °C to 522 °C (Fig. S5 and S6a),

indicating the high catalytic activity of LSCO perovskite. By applying a nanoarray configuration, high dispersion of LSCO and increased close contact between soot and LSCO catalyst can be achieved, resulting low temperature soot oxidation at 477 °C (Fig. 4b). On the contrary, LSCO-ZnO powder form configuration shows high temperature soot oxidation around 580 °C (Fig. S6a) due to a lack of easy accessibility and contacting between LSCO catalyst and soot. Therefore, both LSCO perovskite and ZnO nanoarray well defined 3D structure play important role for realizing a non-precious metal based low temperature soot oxidation catalyst.

Further improvement of the nanorod array-based catalysts for soot oxidation can be achieved by Strontium doping (Fig. 4c). Higher doping ratio of Sr leads to lower soot oxidation temperature at the maximum soot conversion. Soot oxidation over blank ZnO nanorod array is also performed and used as the control experiment. Both CO and CO_2 are released during soot oxidation over ZnO, due to its inefficient catalytic activity (Soot to catalyst ratio is kept constant to exclude its effect on CO production as shown in Table 1), whereas only CO_2 is produced during soot oxidation over the nanorod array-based catalysts. In the best-case scenario, the temperature at the maximum soot oxidation conversion is lowered by about 260 °C through Sr doping ($La_{0.4}Sr_{0.6}CoO_3$). The maximum CO_2 formation rate per mass of perovskite reaches the highest when Sr/La ratio is 0.67. Further increase of the Sr/La ratio results in a decrease of the maximum CO_2 formation rate, while a lower oxidation temperature. The decrease in the maximum CO_2 formation rate with increasing Sr/La ratio may be due to the decreasing reaction temperature with increasing Sr/La ratio, resulting in sluggish kinetics and significant drop of O_{obs} species (Table 1, O_{lattic}/O_{obs}).

3.3. Soot oxidation over nanorod array-based forests in NO/O_2

To better understand the catalyst's soot oxidation capability, 200 ppm of NO is added to simulate the passive DPF regeneration conditions. Soot oxidation over LSCO/ZnO nanorod array catalysts in O_2 and NO/O_2 are compared in Fig. 5(a, b). The soot to catalyst weight ratio is kept consistent when switching the catalysts (Table 1), to eliminate the effect of soot loading on oxidation temperature. As shown, in both gas atmospheres, the increased Sr/La doping ratio enhances the catalyst activity in soot oxidation, lowering the oxidation temperatures. The lower temperature peaks in the NO/O_2 atmosphere are attributed to the enhanced soot oxidation by NO_2 [21,48,49]. However, the higher temperature peaks in the NO/O_2 atmosphere, which represent the soot fraction that is oxidized by O_2, show a temperature lag in oxidation

compared to soot oxidation in O_2, particularly in the cases of $La_{0.6}Sr_{0.4}CoO_3$ and $La_{0.8}Sr_{0.2}CoO_3$ where the Sr dopant is in a relatively low concentration. This could be due to the NO_2 formation where active O species are consumed by NO, resulting less available O active species.

Soot oxidation over $La_{0.4}Sr_{0.6}CoO_3$ in O_2 exhibits a shoulder at relatively high temperatures, which is likely due to non-uniformity of the soot loading (localized thick soot cake). This can be verified by changing the soot loadings (Fig. 6a). It should be noted that the localized thick soot cake is probably caused by the method of loading soot used in this study. It means that when soot accumulation reaches to an extent, higher temperatures are required for a significant fraction of soot to be oxidized, consequently compromising the overall performance of the catalysts (Fig. 6a). To apply nanorod array catalysts in the practical exhaust situation, catalyst loading should be tested and adjusted to accommodate the amount of soot produced/accumulated before the exhaust reaches the catalyst functioning temperature. For instance, below 8 wt% of soot should be loaded for the optimum performance based on the catalyst formulated in this work. It is noted that the soot weight percentage is calculated as weight of soot divided by the weight of $La_{0.4}Sr_{0.6}CoO_3/ZnO/SiC$ times 100. The secondary peak at about 500 °C is attributed to the large weight percentage of soot that is not directly contacting catalyst surface and requires higher energy for oxygen to spill over.

The conversion of NO during soot oxidation in NO/O_2 is also examined, compared to NO oxidation without soot (Figs. 5c and 6b). For all the situations studied here, only CO_2 is observed in the outlet exhaust stream. NO conversion is initially increased with temperature, reaching a maximum conversion, while above this certain temperature, it is decreased overlapping with the thermodynamic equilibrium curve, indicating a high reaction kinetics. It is very clear that NO oxidation to NO_2 (Figs. 5c and 6b for nitrogen balance) is promoted by soot and the catalyst formulated, reaching about 75 % maximum NO conversion.

Moreover, it is noted that oxygen mobility (spillover) enhanced by Sr doping is more favorable to soot than the adsorbed NO molecules, when both soot and NO present (Fig. 5c). Bueno [50] performed NO oxidation and soot oxidation separately over the same set of CeO_2 based catalysts, and studied the correlation between the NO oxidation activity and the soot oxidation activity of the catalysts. It was claimed that enhanced NO oxidation by the catalysts could promote the soot oxidation at low temperatures by providing large amount of NO_2 as strong oxidizer. This study agrees that both NO oxidation and soot oxidation are promoted in parallel by the oxygen vacancies of the catalysts [51,52]. But what's newly learnt is that the catalyst effect on NO oxidation could become
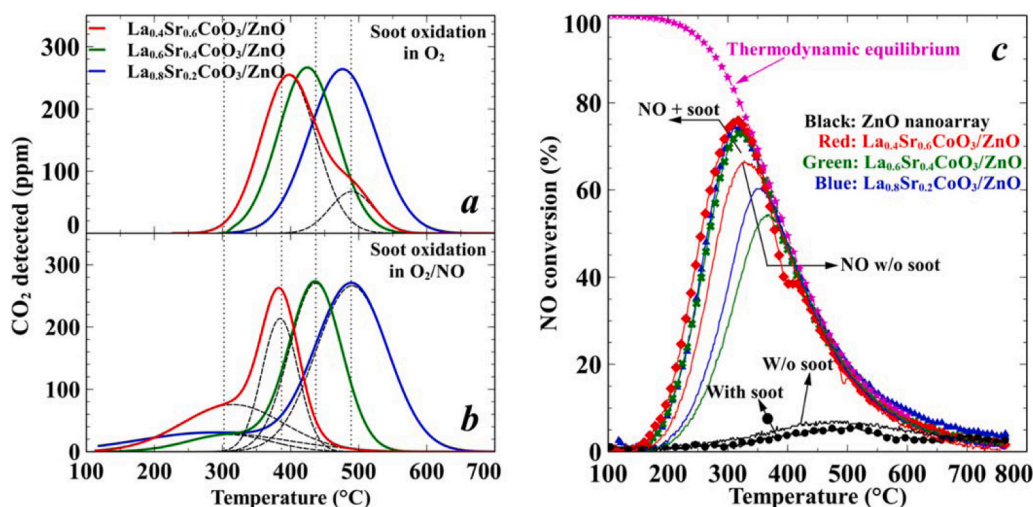

Fig. 5. Soot oxidation over LSCO/ZnO composite nanorod array-based catalysts and control samples in (a) 8 % O_2, compared with that in (b) 200 ppm NO and 8 % O_2. (c) NO oxidation over LSCO/ZnO composite nanorod array-based catalysts, compared with NO and soot co-oxidation. Gas atmosphere: (200 ppm NO), 8 % O_2, balanced in N_2. Thermodynamic equilibrium for NO oxidation was calculated in Aspen Plus using RGibbs Reactor.
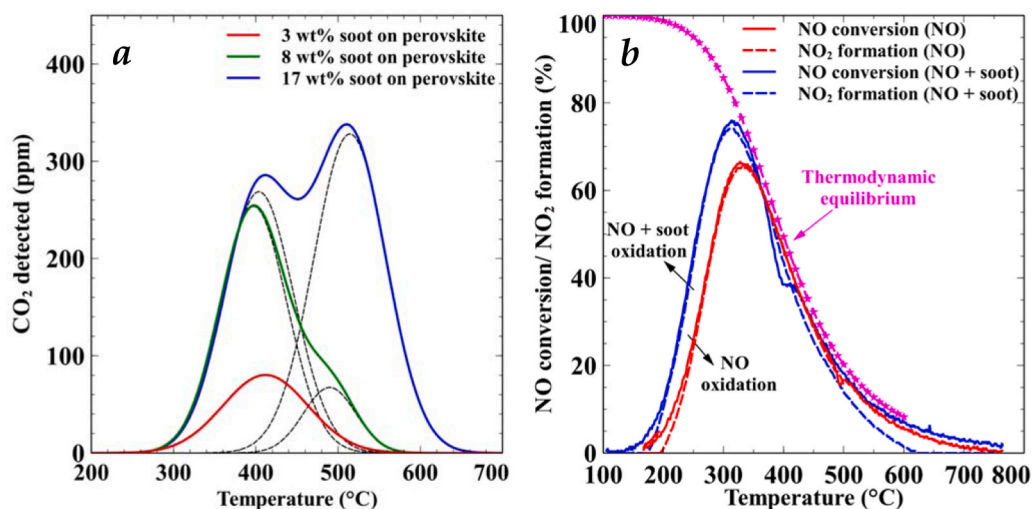
Fig. 6. (a) Effect of soot loading on oxidation performance of the $La_{0.4}Sr_{0.6}CoO_3$/ZnO catalyst. The dashed lines are the deconvoluted curves. (b) Nitrogen balance during NO/soot oxidation and just NO oxidation over $L_{0.4}S_{0.6}CO$/ZnO nanorod array-based catalyst.

different when soot is present (Fig. 5c, NO conversion with and without soot). When soot is absent, NO conversion increases with the increase of Sr doping, while NO conversion stays almost unchanged for all the catalysts with soot involved. This could be due to soot-NO competitive oxidation. At least in the catalyst system used in this study, NO_2 production is not affected by the Sr doping in the catalysts during soot oxidation in NO/O_2 (Fig. 5c), possibly due to the active oxygen species preferable adsorption on soot [53,54].

XPS characterizations are performed to better understand the Sr doping enhanced soot oxidation. An XPS study (Figs. 7 and 8, and Table 1) shows that this is because the Strontium doping increases the chemisorbed surface oxygen to lattice oxygen ratio, originated from the increased level of oxygen vacancy [25,55]. The weakly superficial chemisorbed oxygen active species play an important role in soot oxidation over perovskite catalysts. In O_2, the active surface oxygens spill/transfer over the soot leading to formation of CO_2 which then desorbs in the gas phase [56]; surface vacancy is readily replenished by gaseous O_2 with regeneration of surface-active oxygen (Mars Van Krevelen type). The key role of catalyst-soot interface region and therefore of the catalyst-soot contact has been demonstrated to be strongly involved in the dynamic reaction process promoting the oxygen transfer

rate at much lower temperatures [57]. In the presence of NO in the gas atmosphere, NO adsorbs on the catalyst surface, reacting with the surface oxygen, forming NO_2. This reaction is promoted by the surface-active oxygen, which also promotes soot oxidation. The formed NO_2 can oxidize soot at a lower temperature, forming NO and leading to a "NO recycling" (Fig. 1c).

On the other hand, the oxygen vacancies within the perovskite lattice generated by Sr doping due to charge compensation also cause the cobalt oxidation state to decrease [58], although the extent of the decrease is small as reflected from XPS. The cobalt oxidation state change was confirmed by temperature programmed reduction (TPR) in Fig. S7. Three major reduction stages were observed for all catalysts. The first stage (350–400 °C) is ascribed to partial reduction of the metallic cation $Co^{3+, 4+}$ into Co^{2+}, whereas the third one (500–600 °C) is ascribed to reduction of Co^{2+} into Co^0 [59]. The second stage represents an intermediate phase of Co, which cannot be clearly identified in this study. The first reduction step is a sign of high intrinsic oxygen reactivity, which can be indicated as a critical factor for soot oxidation. When Sr doping is increased, the first reduction peak shifts to lower temperatures. This phenomenon is attributed to the existence of Co^{4+} ions when La^{3+} ions are partially replaced by Sr^{2+} ions [60]. A clearer peak shift happens at the third stage, where the peak shifts to lower temperatures when the Sr doping is increased, meaning that greater Co^{2+}/Co^{3+} ratio (identified by XPS) leads to enhanced oxygen mobility from bulk to surface and a remarkable surface reactivity towards reduction. The change of the surface state of Co can be viewed as an additional source of oxygen for carbon oxidation towards CO_2.

3.4. Soot oxidation over hydrothermal aged catalysts under simulated exhaust gas conditions

As noted, all the tests and characterizations aforementioned are based on freshly synthesized catalysts. To evaluate the catalysts' performance in more practical scenarios, based on the $La_{0.4}Sr_{0.6}CoO_3$ formula, a hydrothermal aging process is carried out at 650 °C for 120 h following the US Drive protocol [39]. XRD, SEM, TEM, XPS and TPR are utilized to characterize the changes after hydrothermal aging. Based on these hydrothermal aged catalysts, soot oxidation under 6 % of water added condition is conducted. In-situ DRIFTS study is also performed to shed light on the mechanism of soot oxidation under H_2O and NO atmosphere.

As shown in Fig. 9a, CO_2 production from soot oxidation with the hydrothermal aged catalyst shows a bell shape profile with maximum CO_2 production rate at 542 °C. Compared to the freshly made
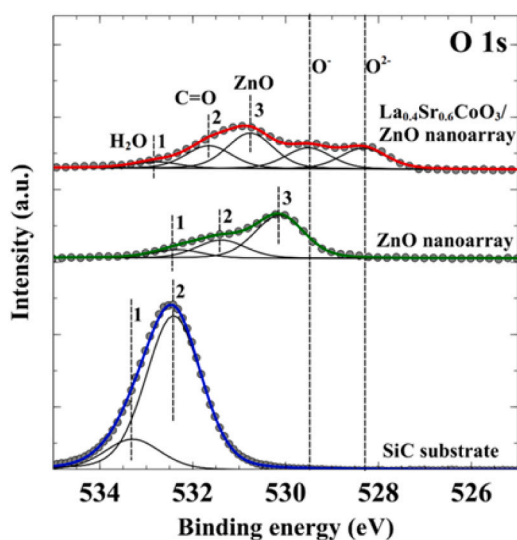

Fig. 7. XPS O 1s results from SiC substrate and ZnO nanorod array on SiC as baselines, compared to that from a LSCO/ZnO/SiC catalyst.
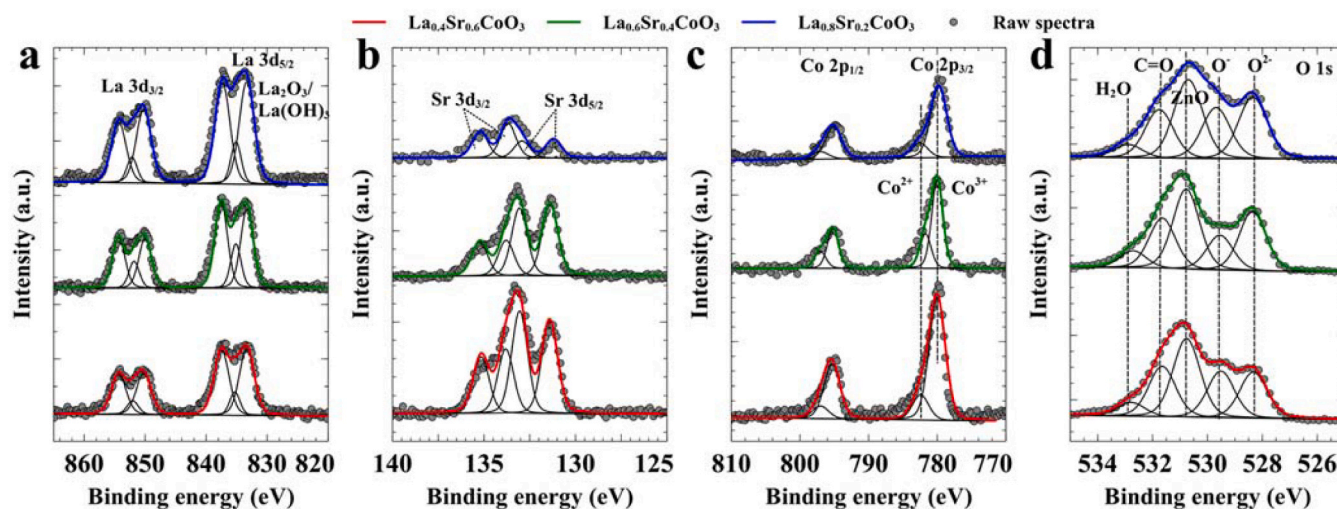
Fig. 8. XPS analyses of the ZnO nanoarray supported $La_{0.4}Sr_{0.6}CoO_3$ catalysts: (a) La 3d, (b) Sr 3d, (c) Co 2p, (d) O 1s.
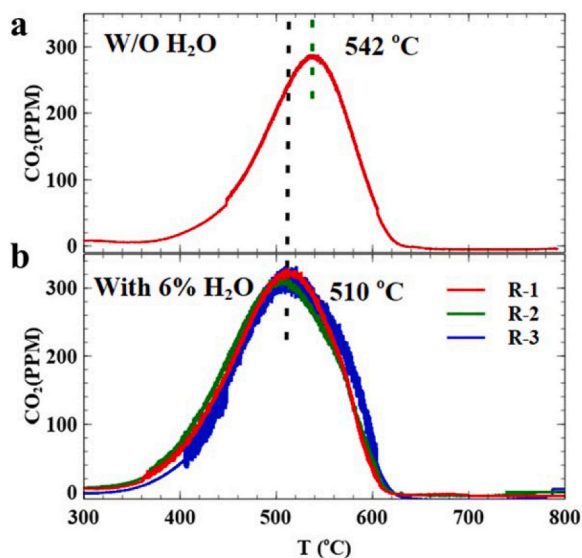

Fig. 9. Hydrothermally aged ZnO nanoarray supported $La_{0.4}Sr_{0.6}CoO_3$ catalyst soot oxidation (a). No water addition. (b). 6 % of H_2O addition.

$La_{0.4}Sr_{0.6}CoO_3$ (Fig. 5a), the T_{max} increased about 100 °C. Nevertheless, the temperature still is ~100 °C lower than that from the Pt commercial catalyst (Fig. 4b). The T_{max} increase is mainly due to the decreased surface-active oxygen species and Co^{3+} (Fig. S12 and Table 1) which are induced by high temperature treatment. This can also be verified by the TPR result which shows a huge decrease for the third reduction peak (Fig. S8a). However, NO oxidation with and without soot seems to be not affected by this change (Fig. S9), indicating a more complicated NO oxidation mechanism. It is interesting that the perovskite crystallite size and phases show negligible change after hydrothermal aging (Fig. S8b and Table 1). Besides, the ZnO-LSCO core-shell structure and LSCO uniform distribution are retained (Fig. S10 and S11), indicating robust physical properties of the nanoarray design. The high stability of the catalyst is also demonstrated through tests under moist conditions, as shown in Fig. 9b. 6 % of water is added for soot oxidation, the catalyst shows nearly no degradation in terms of the CO_2 production after three rounds of testing at temperature up to 800 °C. It is interesting to notice that the T_{max} has a shift to lower temperature at 510 °C, a 32 °C decrease compared with soot oxidation without water. This clearly indicates a water promotion effect for soot oxidation, highly agrees with recent

reports on water effect for soot oxidation [16,61,62].

To understand the mechanism behind the water and NO promotion effect, in-situ DRIFTS study is performed. Shown in Fig. 10b, NO_2 tends to form at around 300 °C and adsorbs on the catalyst surface. The adsorbed NO_2 seems to be the only active N related species (evidenced by Fig. 10a, oxygen only adsorption). While, water tends to be adsorbed and dissociated into -OH species (Fig. 10c, 3500–4000 cm^{-1}). Since -OH species are more oxidative than O_2 [62], it is rational that soot oxidation is promoted under water addition, especially with the case that soot and water have no competitive adsorption. What is more interesting is that the -OH formation is independent of the catalyst surface and interface. Nearly identical -OH species can be observed for SiC-ZnO, SiC-ZnO/LSCO and soot loaded SiC-ZnO/LSCO samples. Even with KBr only, there are still a plenty of -OH species formed.

Based on the results, the soot oxidation mechanism under O_2, water and NO gas atmosphere can be proposed and illustrate in Fig. 10d. Soot oxidation goes through three different pathways simultaneously as following:

I. Soot oxidation with O_2. During this process, O_2 will be firstly adsorbed on LSCO oxygen vacancy and dissociated into active O* species. For close contacted soot oxidation, the O* can easily spill over to the nearby soot surface for CO_2 generation. While, the active O* species need to travel a long distance to reach loose contacted soot surface for oxidation, resulting in a higher oxidation temperature.

II. Soot oxidation promoted with NO_2. NO_2 will be firstly generated from the oxidation of NO. As a stronger oxidant compared to O_2, soot will be oxidized by NO_2 prior to O_2. NO will be generated and participate in the next redox cycle. Diffusion barrier applies for NO_2 promoted loose contact soot oxidation.

III. Soot oxidation promoted with OH group. H_2O can be easily adsorbed and dissociated on both soot and LSCO surface, forming strong OH oxidant species (as proved from the in-situ DRIFTS study). C will react with -OH species and form CO_2. This is reasonable, since adsorption of H_2O on clean catalyst and soot surface shows more negative adsorption energy compared with its adsorption on oxygen vacancy [16].

4. Conclusions

Metal oxide/perovskite based composite nanorod array forest has been successfully integrated onto wall-flow structured SiC honeycomb, forming a new type of energy-efficient and cost-effective catalyzed DPF.
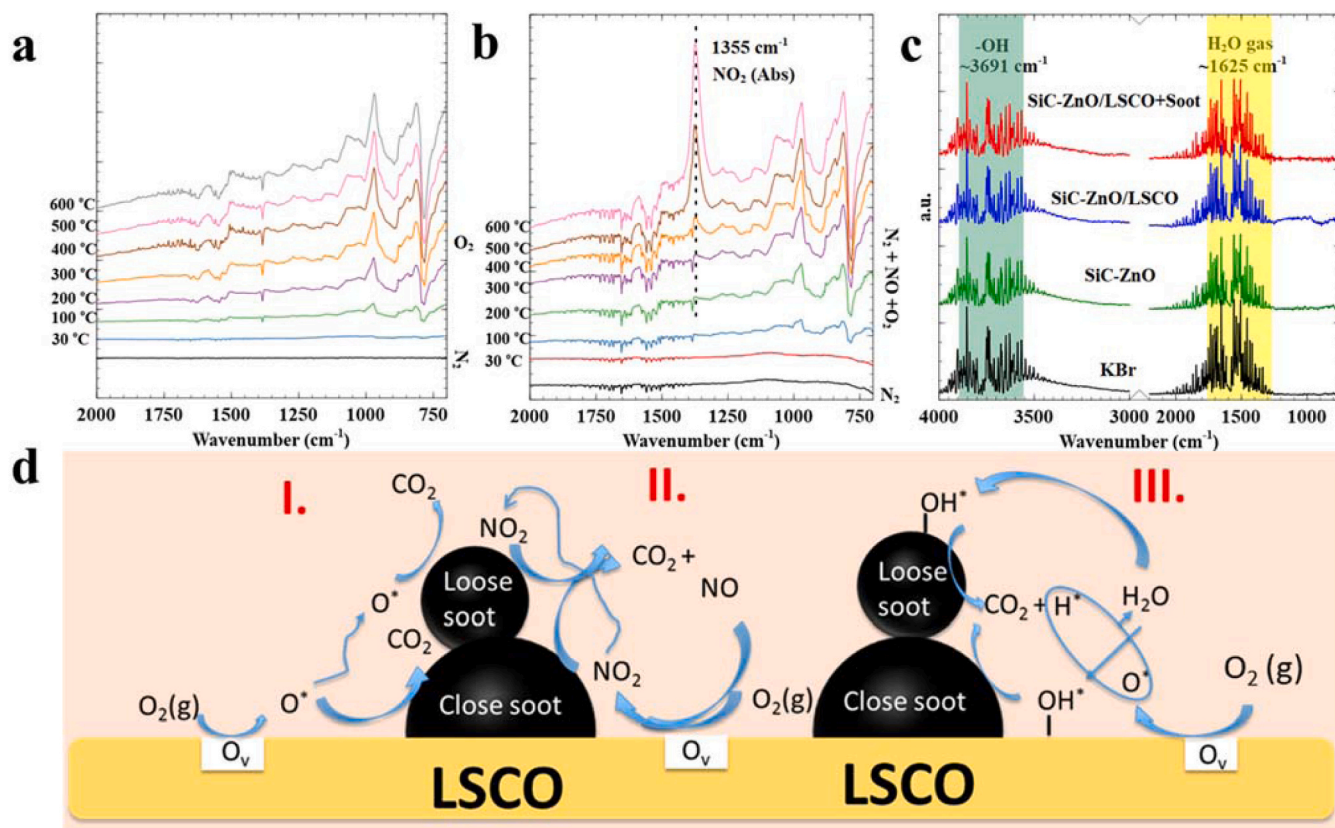
Fig. 10. In situ DRIFTs study for hydrothermally aged $La_{0.4}Sr_{0.6}CoO_3$ catalyst under (a) 8 % of O_2 at different temperatures, (b) 8 % of O_2 with 200 ppm NO at different temperatures. (c) 3 % of H_2O addition with KBr, SiC-ZnO, SiC-ZnO/LSCO and soot loaded SiC-ZnO/LSCO at 500 °C and (d) Proposed soot reaction mechanism.

The nanoarray forests allow three-dimensional tight contact with soot, as well as good dispersion of active PGM-free perovskite catalyst. Besides, the catalyst redox properties can be easily tuned with varied Sr doping. High Sr/La doping ratio tends to increase the surface-active oxygen species, thus lowering soot oxidation temperature. The LSCO/ZnO nanorod array catalysts have shown excellent soot oxidation performance at low temperatures under both O_2 and NO/O_2 atmospheres. The catalyst shows excellent stability and activity even after 120 h of hydrothermal aging at 650 °C. What is more, soot oxidation T_{max} is lowered from 542 °C to 510 °C with 6 % of water steam addition. Such a water promotion effect is due to the formation of more oxidative -OH species over molecular oxygen, which occurs on various surfaces and interfaces, potentially a generic promotion strategy for solid/solid contact oxidation reactions. This work offers a rational catalyst design based on soot-catalyst contact mode controlling and catalyst redox property tuning. The nanoarray supported perovskite catalyst shows great promise for low temperature soot oxidation with reduced cost and prolonged stability. Looking forward, it is noted that the soot oxidation performance using the 3D array catalysts will need be tested under more practical conditions namely, real gas atmosphere and soot loading conditions etc., in order to be further investigated and understood in their performance merits and functional mechanisms, toward the realistic applications of this new type of nanoarray catalysts.

CRediT authorship contribution statement

Chunxiang Zhu: Data curation, Formal analysis, Investigation, Methodology, Software, Validation, Writing - original draft, Writing - review & editing. **Shoucheng Du:** Data curation, Formal analysis, Investigation, Methodology, Software, Validation, Writing - original draft, Writing - review & editing. **Sibo Wang:** Investigation,

Methodology, Data curation. **Xingxu Lu:** Investigation, Methodology, Data curation. **Mingwan Zhang:** Investigation, Data curation. **Bo Zhang:** Investigation, Data curation. **Fangyuan Liu:** Investigation, Data curation. **Wen Xiao:** Investigation, Data curation. **Yanbing Guo:** Investigation, Validation. **Jun Ding:** Investigation, Validation. **Zhaoliang Zhang:** Investigation, Validation. **Pu-Xian Gao:** Funding acquisition, Project administration, Supervision, Investigation, Validation, Writing - review & editing.

Declaration of Competing Interest

The authors declare that they have no known competing financial interests or personal relationships that could have appeared to influence the work reported in this paper.

Data Availability

Data will be made available on request.

Appendix A. Supporting information

Supplementary data associated with this article can be found in the

online version at doi:10.1016/j.apcatb.2023.123336.

References

[1] C. Zhang, D. Yu, C. Peng, L. Wang, X. Yu, Y. Wei, J. Liu, Z. Zhao, Research progress on preparation of 3DOM-based oxide catalysts and their catalytic performances for the combustion of diesel soot particles, Appl. Catal. B 319 (2022), https://doi.org/10.1016/j.apcatb.2022.121946.

[2] Neha, R. Prasad, S.V. Singh, A review on catalytic oxidation of soot emitted from diesel fueled engines, J. Environ. Chem. Eng. 8 (2020), https://doi.org/10.1016/j.jece.2020.103945.

[3] M. Williams, R. Minjares, A technical summary of Euro 6/VI vehicle emission standards (2016) www.theicct.org.

[4] C. Bischof, T. Boger, N. Gunasekarari, R. Bhargava, Advanced particulate filter technologies for direct injection gasoline engine applications, Adv. Engine Des. Perform. 73 (2013) 298–303.

[5] J. Luo, Y. Tie, L. Tang, Y. Li, H. Xu, Z. Liu, M. Li, H. Zhang, Z. Zhang, Effect of regeneration method and ash deposition on diesel particulate filter performance: a review, Environ. Sci. Pollut. Res. (2023), https://doi.org/10.1007/s11356-023-25880-2.

[6] J. Lee, J.R. Theis, E.A. Kyriakidou, Vehicle emissions trapping materials: successes, challenges, and the path forward, Appl. Catal. B 243 (2019) 397–414, https://doi.org/10.1016/j.apcatb.2018.10.069.

[7] D. Fino, S. Bensaid, M. Piumetti, N. Russo, A review on the catalytic combustion of soot in Diesel particulate filters for automotive applications: from powder catalysts to structured reactors, Appl. Catal. A Gen. 509 (2016) 75–96, https://doi.org/10.1016/j.apcata.2015.10.016.

[8] M.Y. Kim, E.A. Kyriakidou, J.S. Choi, T.J. Toops, A.J. Binder, C. Thomas, J.E. Parks, V. Schwartz, J. Chen, D.K. Hensley, Enhancing low-temperature activity and durability of Pd-based diesel oxidation catalysts using ZrO2 supports, Appl. Catal. B 187 (2016) 181–194, https://doi.org/10.1016/j.apcatb.2016.01.023.

[9] Q. Wu, M. Jing, Y. Wei, Z. Zhao, X. Zhang, J. Xiong, J. Liu, W. Song, J. Li, High-efficient catalysts of core-shell structured Pt@transition metal oxides (TMOs) supported on 3DOM-Al2O3 for soot oxidation: the effect of strong Pt-TMO interaction, Appl. Catal. B 244 (2019) 628–640, https://doi.org/10.1016/j.apcatb.2018.11.094.

[10] R. Matarrese, L. Castoldi, L. Lietti, P. Forzatti, Soot combustion: Reactivity of alkaline and alkaline earth metal oxides in full contact with soot, Catal. Today 136 (2008) 11–17, https://doi.org/10.1016/j.cattod.2008.03.022.

[11] E. Aneggi, C. de Leitenburg, G. Dolcetti, A. Trovarelli, Diesel soot combustion activity of ceria promoted with alkali metals, Catal. Today 136 (2008) 3–10, https://doi.org/10.1016/j.cattod.2008.01.002.

[12] X. Mei, J. Xiong, Y. Wei, Y. Zhang, P. Zhang, Q. Yu, Z. Zhao, J. Liu, High-efficient non-noble metal catalysts of 3D ordered macroporous perovskite-type La2NiB'O6 for soot combustion: Insight into the synergistic effect of binary Ni and B' sites, Appl. Catal. B 275 (2020), https://doi.org/10.1016/j.apcatb.2020.119108.

[13] L. Zeng, L. Cui, C. Wang, W. Guo, C. Gong, In-situ modified the surface of Pt-doped perovskite catalyst for soot oxidation, J. Hazard Mater. 383 (2020), 121210, https://doi.org/10.1016/j.jhazmat.2019.121210.

[14] C. Lee, Y. Jeon, S. Hata, J. Park Il, R. Akiyoshi, H. Saito, Y. Teraoka, Y.G. Shul, H. Einaga, Three-dimensional arrangements of perovskite-type oxide nano-fiber webs for effective soot oxidation, Appl. Catal. B 191 (2016) 157–164, https://doi.org/10.1016/j.apcatb.2016.03.001.

[15] J. Xiong, X. Mei, J. Liu, Y. Wei, Z. Zhao, Z. Xie, J. Li, Efficiently multifunctional catalysts of 3D ordered meso-macroporous Ce0.3Zr0.7O2-supported Pd-Au-CeO2 core-shell nanoparticles for soot oxidation: Synergetic effect of Pd-Au-CeO2 ternary components, Appl. Catal. B 251 (2019) 247–260, https://doi.org/10.1016/j.apcatb.2019.03.078.

[16] C. Sun Park, M.W. Lee, J.H. Lee, E.J. Jeong, S.H. Lee, J.W. Choung, C.H. Kim, H.C. Ham, K.Y. Lee, Promoting effect of H2O over macroporous Ce-Zr catalysts in soot oxidation, Mol. Catal. 474 (2019), 110416, https://doi.org/10.1016/j.mcat.2019.110416.

[17] J. Xiong, Q. Wu, X. Mei, J. Liu, Y. Wei, Z. Zhao, D. Wu, J. Li, Fabrication of spinel-Type PdxCo3- xO4 binary active sites on 3D ordered meso-macroporous Ce-Zr-O2 with enhanced activity for catalytic soot oxidation, ACS Catal. 8 (2018) 7915–7930, https://doi.org/10.1021/acscatal.8b01924.

[18] D. Yu, Y. Ren, X. Yu, X. Fan, L. Wang, R. Wang, Z. Zhao, K. Cheng, Y. Chen, Z. Sojka, A. Kotarba, Environmental Facile synthesis of birnessite-type K 2 Mn 4 O 8 and cryptomelane-type K 2-x Mn 8 O 16 catalysts and their excellent catalytic performance for soot combustion with high resistance to H 2 O and SO 2, Appl. Catal. B 285 (2021), https://doi.org/10.1016/j.apcatb.2020.119779.

[19] D. Yu, L. Wang, C. Zhang, C. Peng, X. Yu, X. Fan, B. Liu, K. Li, Z. Li, Y. Wei, J. Liu, Z. Zhao, Alkali metals and cerium-modified La-Co-based perovskite catalysts: facile synthesis, excellent catalytic performance, and reaction mechanisms for soot combustion, ACS Catal. 12 (2022) 15056–15075, https://doi.org/10.1021/acscatal.2c03418.

[20] V. Torregrosa-Rivero, M.S. Sánchez-Adsuar, M.J. Illán-Gómez, Analyzing the role of copper in the soot oxidation performance of BaMnO3-perovskite-based catalyst obtained by modified sol-gel synthesis, Fuel 328 (2022), https://doi.org/10.1016/j.fuel.2022.125258.

[21] Q.N. Tran, F. Martinovic, M. Ceretti, S. Esposito, B. Bonelli, W. Paulus, F. Di Renzo, F.A. Deorsola, S. Bensaid, R. Pirone, Co-doped LaAlO3 perovskite oxide for NOx-assisted soot oxidation, Appl. Catal. A Gen. 589 (2020), https://doi.org/10.1016/j.apcata.2019.117304.

[22] J.H. Lee, S.H. Lee, J.W. Choung, C.H. Kim, K.Y. Lee, Ag-incorporated macroporous CeO2 catalysts for soot oxidation: effects of Ag amount on the generation of active oxygen species, Appl. Catal. B 246 (2019) 356–366, https://doi.org/10.1016/j.apcatb.2019.01.064.

[23] F. Fang, P. Zhao, N. Feng, C. Chen, X. Li, G. Liu, H. Wan, G. Guan, Construction of a hollow structure in La0.9K0.1CoO3-: δ nanofibers via grain size control by Sr substitution with an enhanced catalytic performance for soot removal, Catal. Sci. Technol. 9 (2019) 4938–4951, https://doi.org/10.1039/c9cy01332f.

[24] H. Wang, C. Chen, Y. Zhang, L. Peng, S. Ma, T. Yang, H. Guo, Z. Zhang, D.S. Su, J. Zhang, In situ oxidation of carbon-encapsulated cobalt nanocapsules creates highly active cobalt oxide catalysts for hydrocarbon combustion, Nat. Commun. 6 (2015) 2–7, https://doi.org/10.1038/ncomms8181.

[25] E. Aneggi, V. Rico-Perez, C. De Leitenburg, A. Maschio, L. Soler, J. Llorca, A. Trovarelli, Ceria-zirconia particles wrapped in a 2D carbon envelope: improved low-temperature oxygen transfer and oxidation activity, Angew. Chem. - Int. Ed. 54 (2015) 14040–14043, https://doi.org/10.1002/anie.201507839.

[26] Y. Guo, Z. Ren, W. Xiao, C. Liu, H. Sharma, H. Gao, A. Mhadeshwar, P.X. Gao, Robust 3-D configurated metal oxide nano-array based monolithic catalysts with ultrahigh materials usage efficiency and catalytic performance tunability, Nano Energy 2 (2013) 873–881, https://doi.org/10.1016/j.nanoen.2013.03.004.

[27] J. Weng, P.X. Gao, Z. Gao, J. Pihl, T. LaClair, M. Zhang, K. Gluesenkamp, A. Momen, Nanoarray-based monolithic adsorbers for SO2 removal, Emiss. Control Sci. Technol. 6 (2020) 315–323, https://doi.org/10.1007/s40825-020-00161-3.

[28] Z. Ren, Y. Guo, P.X. Gao, Nano-array based monolithic catalysts: concept, rational materials design and tunable catalytic performance, Catal. Today 258 (2015) 441–453, https://doi.org/10.1016/j.cattod.2015.01.033.

[29] B. Zhang, J. Sun, U. Salahuddin, P.X. Gao, Hierarchical and scalable integration of nanostructures for energy and environmental applications: a review of processing, devices, and economic analyses, Nano Futures 4 (2020) 1–37, https://doi.org/10.1088/2399-1984/ab75ad.

[30] S. Wang, Z. Ren, Y. Guo, P.X. Gao, Nano-array integrated monolithic devices: toward rational materials design and multi-functional performance by scalable nanostructures assembly, CrystEngComm 18 (2016) 2980–2993, https://doi.org/10.1039/c6ce00342g.

[31] X. Lu, M. Li, S. Hoang, S.L. Suib, P.X. Gao, Solvent effects on the heterogeneous growth of TiO2 nanostructure arrays by solvothermal synthesis, Catal. Today 360 (2021) 275–283, https://doi.org/10.1016/j.cattod.2020.02.044.

[32] T. Liu, Q. Li, Y. Xin, Z. Zhang, X. Tang, L. Zheng, P.X. Gao, Quasi free K cations confined in hollandite-type tunnels for catalytic solid (catalyst)-solid (reactant) oxidation reactions, Appl. Catal. B 232 (2018) 108–116, https://doi.org/10.1016/j.apcatb.2018.03.049.

[33] S. Wang, Z. Ren, W. Song, Y. Guo, M. Zhang, S.L. Suib, P.X. Gao, ZnO/perovskite core-shell nanorod array based monolithic catalysts with enhanced propane oxidation and material utilization efficiency at low temperature, Catal. Today 258 (2015) 549–555, https://doi.org/10.1016/j.cattod.2015.03.026.

[34] S. Hoang, Y. Guo, A.J. Binder, W. Tang, S. Wang, J. (Jimmy) Liu, T.D. Huan, X. Lu, Y. Wang, Y. Ding, E.A. Kyriakidou, J. Yang, T.J. Toops, T.J. Pauly, R. Ramprasad, P.X. Gao, Activating low-temperature diesel oxidation by single-atom Pt on TiO2 nanowire array, Nat. Commun. 11 (2020), https://doi.org/10.1038/s41467-020-14816-w.

[35] Y. Guo, Z. Ren, W. Xiao, C. Liu, H. Sharma, H. Gao, A. Mhadeshwar, P.X. Gao, Robust 3-D configurated metal oxide nano-array based monolithic catalysts with ultrahigh materials usage efficiency and catalytic performance tunability, Nano Energy 2 (2013) 873–881, https://doi.org/10.1016/j.nanoen.2013.03.004.

[36] S. Du, S. Wang, Y. Guo, X. Lu, W. Tang, Y. Ding, X. Mao, P.X. Gao, Rational design, synthesis and evaluation of ZnO nanorod array supported Pt:La0.8Sr0.2MnO3 lean NOx traps, Appl. Catal. B 236 (2018) 348–358, https://doi.org/10.1016/j.apcatb.2018.05.007.

[37] X. Lu, W. Tang, M. Li, Y. Dang, N. Campbell, Z. Li, S.L. Suib, P.X. Gao, Mass transport in nanoarray monolithic catalysts: An experimental-theory study, Chem. Eng. J. 405 (2021), https://doi.org/10.1016/j.cej.2020.126906.

[38] W. Tang, X. Lu, F. Liu, S. Du, J. Weng, S. Hoang, S. Wang, C.Y. Nam, P.X. Gao, Ceria-based nanoflake arrays integrated on 3D cordierite honeycombs for efficient low-temperature diesel oxidation catalyst, Appl. Catal. B 245 (2019) 623–634, https://doi.org/10.1016/j.apcatb.2019.01.028.

[39] ACEC Technical Team, Aftertreatment Protocols for Catalyst Characterization and Performance Evaluation: Low-Temperature Oxidation Catalyst Test Protocol, 2015.

[40] S. Du, W. Tang, Y. Guo, A. Binder, E.A. Kyriakidou, T.J. Toops, S. Wang, Z. Ren, S. Hoang, P.X. Gao, Understanding low temperature oxidation activity of nanoarray-based monolithic catalysts: from performance observation to structural and chemical insights, Emiss. Control Sci. Technol. 3 (2017) 18–36, https://doi.org/10.1007/s40825-016-0054-y.

[41] X. Lu, Y. Dang, M. Li, C. Zhu, F. Liu, W. Tang, J. Weng, M. Ruan, S.L. Suib, P.X. Gao, Synergistic promotion of transition metal ion-exchange in TiO2 nanoarray-based monolithic catalysts for the selective catalytic reduction of NOx with NH3, Catal. Sci. Technol. 12 (2022) 5397–5407, https://doi.org/10.1039/d2cy00996j.

[42] J. Sun, F. Liu, U. Salahuddin, M. Wu, C. Zhu, X. Lu, B. Zhang, B. Zhao, Z. Xie, Y. Ding, D. Li, C.Y. Nam, F.Y. Zhang, P.X. Gao, Optimization and understanding of ZnO nanoarray supported Cu-ZnO-Al2O3 catalyst for enhanced CO2 -methanol conversion at low temperature and pressure, Chem. Eng. J. (2022), https://doi.org/10.1016/j.cej.2022.140559.

[43] J.C. Dupin, D. Gonbeau, P. Vinatier, A. Levasseur, Systematic XPS studies of metal oxides, hydroxides and peroxides, Phys. Chem. Chem. Phys. 2 (2000) 1319–1324, https://doi.org/10.1039/a908800h.

[44] P.A.W. van der Heide, Systematic x-ray photoelectron spectroscopic study of La1−xSrx-based perovskite-type oxides.pdf, Surf. Interface Anal. 33 (2002) 414–425, https://doi.org/10.1002/sia.1227.

[45] W. Zang, Y. Nie, D. Zhu, P. Deng, L. Xing, X. Xue, Core-shell In2O3/ZnO nanoarray nanogenerator as a self-powered active gas sensor with high H2S sensitivity and selectivity at room temperature, J. Phys. Chem. C 118 (2014) 9209–9216, https://doi.org/10.1021/jp500516t.

[46] N. Müller, R. Moos, A. Jess, In situ monitoring of coke deposits during coking and regeneration of solid catalysts by electrical impedance-based sensors, Chem. Eng. Technol. 33 (2010) 103–112, https://doi.org/10.1002/ceat.200900380.

[47] X. Mao, S. Liu, W. Liu, X. Wu, S. Liu, A simple model catalyst study to distinguish the roles of different oxygen species in propane and soot combustion, Appl. Catal. B 310 (2022), https://doi.org/10.1016/j.apcatb.2022.121331.

[48] X. Wang, B. Jin, R. Feng, W. Liu, D. Weng, X. Wu, S. Liu, A robust core-shell silver soot oxidation catalyst driven by Co3O4: Effect of tandem oxygen delivery and Co3O4-CeO2 synergy, Appl. Catal. B 250 (2019) 132–142, https://doi.org/10.1016/j.apcatb.2019.03.019.

[49] X. Yu, Y. Ren, D. Yu, M. Chen, L. Wang, R. Wang, X. Fan, Z. Zhao, K. Cheng, Y. Chen, J. Gryboś, A. Kotarba, Z. Sojka, Y. Wei, J. Liu, Hierarchical porous K-OMS-2/3DOM-m Ti0.7Si0.3O2 catalysts for soot combustion: Easy preparation, high catalytic activity, and good resistance to H2O and SO2, ACS Catal. 11 (2021) 5554–5571, https://doi.org/10.1021/acscatal.1c00748.

[50] N. Guillén-Hurtado, A. García-García, A. Bueno-López, Isotopic study of ceria-catalyzed soot oxidation in the presence of NOx, J. Catal. 299 (2013) 181–187, https://doi.org/10.1016/j.jcat.2012.11.026.

[51] J.O. Müller, B. Frank, R.E. Jentoft, R. Schlögl, D.S. Su, The oxidation of soot particulate in the presence of NO 2, Catal. Today 191 (2012) 106–111, https://doi.org/10.1016/j.cattod.2012.03.010.

[52] Z. Li, M. Meng, Y. Zha, F. Dai, T. Hu, Y. Xie, J. Zhang, Highly efficient multifunctional dually-substituted perovskite catalysts La 1-xK xCo 1-yCu yO 3-δ used for soot combustion, NOx storage and simultaneous NOx-soot removal, Appl. Catal. B 121–122 (2012) 65–74, https://doi.org/10.1016/j.apcatb.2012.03.022.

[53] S. Liu, X. Wu, H. Luo, D. Weng, R. Ran, Pt/Zeolite catalysts for soot oxidation: influence of hydrothermal aging, J. Phys. Chem. C. 119 (2015) 17218–17227, https://doi.org/10.1021/acs.jpcc.5b04882.

[54] S. Liu, X. Wu, D. Weng, M. Li, R. Ran, Roles of acid sites on Pt/H-ZSM5 catalyst in catalytic oxidation of diesel soot, ACS Catal. 5 (2015) 909–919, https://doi.org/10.1021/cs5018369.

[55] L. Zhong, F. Hai, P. Xiao, J. Hong, J. Zhu, Improved low-temperature activity of La-Sr-Co-O nano-composite for CO oxidation by phase cooperation, RSC Adv. 4 (2014) 61476–61481, https://doi.org/10.1039/c4ra10902c.

[56] D. Fino, N. Russo, G. Saracco, V. Specchia, The role of suprafacial oxygen in some perovskites for the catalytic combustion of soot, J. Catal. 217 (2003) 367–375, https://doi.org/10.1016/S0021-9517(03)00143-X.

[57] S. Zhang, X. Feng, C. Rao, X. Xu, J. Xu, X. Fang, Y. Li, X. Wang, Engineering low Pd content catalysts for soot combustion through tuning the Pd-SnO2 interface interaction: Disclosing the critical role of dual Pd valence states for the activity, Appl. Catal. A Gen. 647 (2022), https://doi.org/10.1016/j.apcata.2022.118906.

[58] X. Wang, K. Huang, L. Yuan, S. Xi, W. Yan, Z. Geng, Y. Cong, Y. Sun, H. Tan, X. Wu, L. Li, S. Feng, Activation of surface oxygen sites in a cobalt-based Perovskite model catalyst for CO oxidation, J. Phys. Chem. Lett. 9 (2018) 4146–4154, https://doi.org/10.1021/acs.jpclett.8b01623.

[59] X. Wang, K. Huang, L. Yuan, S. Li, W. Ma, Z. Liu, S. Feng, Molten salt flux synthesis, crystal facet design, characterization, electronic structure, and catalytic properties of Perovskite cobaltite, ACS Appl. Mater. Interfaces 10 (2018) 28219–28231, https://doi.org/10.1021/acsami.8b08621.

[60] S. Fang, L. Wang, Z. Sun, N. Feng, C. Shen, P. Lin, H. Wan, G. Guan, Catalytic removal of diesel soot particulates over K and Mg substituted La1−xKxCo 1−yMgyO3 perovskite oxides, Catal. Commun. 49 (2014) 15–19, https://doi.org/10.1016/j.catcom.2014.01.029.

[61] W. Yang, Y. Wang, H. Wang, Y. Zhang, Y. Peng, J. Li, Water accelerates and directly participates soot oxidation: an isotopic study, Appl. Catal. B 302 (2022), https://doi.org/10.1016/j.apcatb.2021.120837.

[62] O.A. Shromova, N.M. Kinnunen, T.A. Pakkanen, M. Suvanto, Promotion effect of water in catalytic fireplace soot oxidation over silver and platinum, RSC Adv. 7 (2017) 46051–46059, https://doi.org/10.1039/c7ra09291a.